RSC Advances

PAPER

View Article Online
View Journal | View Issue



Cite this: *RSC Adv.*, 2025, **15**, 36525

# Design and synthesis of novel angular 4,5-pyranocoumarin fluorescent probes for detecting hydrazine and their applications

Huafeng Zhou,†[a] Jiayong Huang,†[a] Jian Su,[a] Xiaowei Su,[a] Qiujuan Chen,[a] Rui Li,[a] Yuxiao Zheng,[a] Rui Chen*[b] and Lini Huo *[ac]

Received 22nd June 2025
Accepted 27th August 2025

DOI: 10.1039/d5ra04433b

rsc.li/rsc-advances

Novel structured 4,5-pyranocoumarin-based fluorescent probes (**2b** and **3c**) were designed and synthesized for the selective detection of hydrazine hydrate ($N_2H_4$). The probes feature an extended conjugated system *via* a 3-aryl-substituted pyranocoumarin skeleton, with ester groups serving as recognition sites for $N_2H_4$. Probe **3c** demonstrated superior performance, exhibiting a 494% fluorescence enhancement at 460 nm with a detection limit of 0.03 μM, surpassing most reported coumarin-based fluorescent probes for hydrazine detection and the EPA safety threshold. Both probes exhibited high selectivity against 17 interferents (ions/biomolecules) and functioned effectively in complex matrices, including food samples (lettuce, rice) and vapor-phase detection *via* test strips. Probe **3c** achieved rapid (<5 min), pH-stable (pH 6–10) responses with visible color transitions (blue-green to green), while **2b** operated across a broader pH range (1–12). This work highlights pyranocoumarin scaffolds as promising platforms for designing intensity-responsive probes, combining synthetic novelty, sensitivity, and practicality for environmental and food safety.



## 1 Introduction

As a crucial multifunctional chemical reagent, hydrazine hydrate ($N_2H_4$) plays an indispensable role in diverse fields, including chemical synthesis, catalytic processes, pesticide manufacturing, and industrial production.[1–3] However, $N_2H_4$ can enter an organism through skin absorption and inhalation of respiratory mucosa, thereby causing irreversible physiological damage.[4–6] With the acceleration of industrialization, the problem of soil and water pollution caused by improper discharge of hydrazine-containing wastes has become increasingly serious. Consequently, the development of efficient detection methods has become a critical priority for environmental monitoring, industrial safety protocols, and biomedical research.[7,8]

Fluorescent probes are widely recognized for their advantages of simple synthesis, strong selectivity, and good biocompatibility.[9–13] Organic fluorophores such as coumarin derivatives have attracted much attention due to their relatively low toxicity, ease of chemical modification and excellent stability.[14–16] Recent advancements have focused on coumarin probes (**1**–**3**) for hydrazine detection (Fig. 1), with multiple studies reporting pronounced fluorescence enhancement or distinct colorimetric responses upon hydrazine exposure.[17–19]

In the design of probes for detecting $N_2H_4$, functional groups such as aldehydes, ketones, and esters are strategically incorporated to enable selective detection through nucleophilic addition or substitution reactions with hydrazine, inducing measurable fluorescence changes.[17–21] The ester group, recognized as an efficient recognition moiety, has been widely utilized in the detection of hydrazine hydrate.[22–24] Pyranocoumarin, a class of coumarin derivatives featuring a pyran ring, have emerged as ideal candidates for designing fluorescent probes due to their fluorescence properties similar to those of simple coumarins. However, the current research in this field is still relatively limited. Herein, we designed a novel pyranocoumarin skeleton (Fig. 2), bearing an aryl group at the 3-position to effectively extend the coumarin's conjugated plane. Meanwhile, ester groups were introduced at the 7- or 8-positions as hydrazine recognition sites, and the effects of monoester and diester groups on hydrazine recognition were systematically examined. And the spectral properties of the target compounds was conducted using fluorescence and UV-Vis spectrophotometry.

[a]*Guangxi University of Chinese Medicine, Nanning 530222, China. E-mail: huolini@126.com*

[b]*Guangxi Vocational University of Agriculture, 530009, China. E-mail: 58251323@qq.com*

[c]*International College, Krirk University, Bangkok 10220, Thailand*

† These authors have contributed equally.

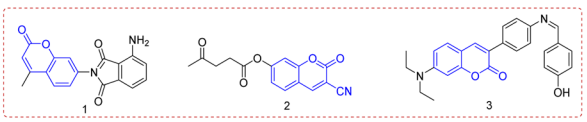


Fig. 1 Coumarin-based probes for hydrazine detection.

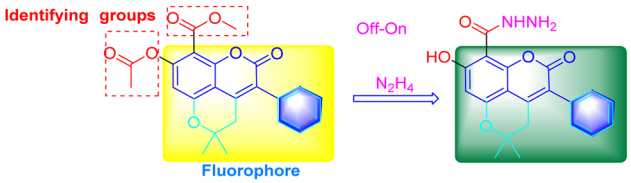


Fig. 2 Rational design strategy for novel pyranocoumarin-based coumarin-based fluorescent probe for hydrazine detection.

## 2 Experimental

### 2.1 Materials and apparatus

All reagents and metal salts used in the experiments were purchased from Aladdin Industrial Corporation (Shanghai, China) or Sigma-Aldrich Trading Co. Ltd (St. Louis, MO, USA).The reagents used in the experiment are all analytically pure. NMR spectra were recorded on a DRX-500 NMR spectrometer (Rheinstetten, Germany), and high-resolution mass spectrometry (HRMS) was performed using an Agilent 6210 ESI/TOF mass spectrometer (Palo Alto, CA, USA). Single-crystal X-ray diffraction (SCXRD) data were collected on an Agilent SuperNova Dual Cu-at-zero AtlasS2 diffractometer (Palo Alto, CA, USA). Fluorescence spectra were measured with a Shimadzu RF-6000 spectrofluorophotometer (Tokyo, Japan). UV-Vis absorption spectra were obtained using a UV-1800P spectrophotometer (Shanghai Meipuda Instrument Co, Ltd, China). pH measurements were conducted with a PHB-1 portable pH meter (Shanghai Shinuo Physical Optical Instrument Co., Ltd, China).

### 2.2 Preparation of the probe

**2.2.1 Preparation of intermediate 1.** Under the action of electromagnetic stirring, 20 mL of anhydrous dioxane, 2.81 g of 2,4,6-trihydroxybenzoic methylester (10 mmol) and 2.26 g of 3,3-dimethylacrylic acid (22 mmol) were added successively to a 50 mL round-bottom flask and heated in an oil bath at 95 °C. The reaction was stirred under reflux for 7 h and TLC was used to monitor the reaction (petroleum ether : ethyl acetate = 4 : 1). The reaction was stirred under reflux for 7 h, and the progress of the reaction was monitored by thin-layer chromatography (TLC) using petroleum ether and ethyl acetate (4 : 1, v/v) as the eluent. After completion of the reaction, the reaction mixture was poured into 100 mL of ice-cold water, and saturated aqueous potassium carbonate solution was added to adjust the pH to neutrality. The resulting mixture was then filtered. The crude product was collected and recrystallized from acetone to afford a pale yellow crystalline solid (compound **1**), with a yield of 90% and a melting point of 140.6–144.1 °C.· $^1$H NMR (600 MHz, $CDCl_3$), $\delta$ (ppm): $\delta$ 14.02 (s, 1H), 12.67 (s, 1H), 5.99 (s, 1H), 3.99 (s, 3H, –$OCH_3$), 2.74 (s, 2H), 1.48 (s, 6H, 2× $CH_3$). $^{13}$C NMR (101 MHz, $CDCl_3$) $\delta$ (ppm): $\delta$ 198.07, 168.46, 166.17, 165.85, 164.67, 98.03, 82.75, 82.62, 81.02, 51.11, 48.33, 27.96. HRMS (ESI): calcd for $C_{13}H_{15}O_6$ $[M + H]^+$: 267.3200, found 267.2490.

**2.2.2 Preparation of probes 2a, 2b, and 2c.** Under $N_2$ protection, 4 mL (40 mmol) of acetic anhydride, 0.266 g (1 mmol) of compound 1 and 1 mmol of substituted phenylacetic acids (1 mmol) were successively added to a 50 mL round-bottom flask. The mixture was heated to 100 °C, and then 0.208 mL (1.5 mmol) of triethylamine was added ,followed by increasing the temperature to 150 ℃. The reaction was stirred under reflux for 2–4 hours, monitored by TLC. After the reaction was completed, the reaction mixture was cooled to room temperature, then 8 mL of water was added. The mixture was extracted with ethyl acetate (3 × 15 mL), the organic layers were combined, dried over anhydrous sodium sulfate, filtered, and concentrated. The residue was purified by column chromatography using petroleum ether and ethyl acetate (4:1, v/v) as the eluent, affording compounds **2a**, **2b**, and **2c** in 40–45% yield.

**2a** (2″,2″-Dimethyl-3-(4′-chlorophenyl)-7-acetoxymethyl-2″*H*,3″*H*-4,5-pyrrolo[3,4-*b*]oxazole-8-carboxylic acid methyl ester) is a white solid, with a yield of 45% and melting range of 216.3–217.5 °C. $^1$H NMR (500 MHz, $CDCl_3$) $\delta$ (ppm): $\delta$ 7.44 (d, $J$ = 7.5 Hz, 2H), 7.24 (d, $J$ = 7.5 Hz, 2H), 6.56 (s, 1H), 3.96 (s, 3H), 2.74 (s, 2H), 2.32 (s, 3H), 1.37 (s, 6H). $^{13}$C NMR (126 MHz, $CDCl_3$) $\delta$ (ppm): $\delta$ 168.67, 163.12, 159.37, 155.38, 152.90, 151.66, 142.29, 134.77, 131.47, 130.54, 128.86, 121.83, 107.52, 107.35, 104.56, 77.51, 52.87, 37.77, 26.44, 20.87. MS (ESI): *m*/*z*, calculated for $C_{22}H_{18}ClO_7Na$ $[M + Na]^+$: 465.0707, found 465.8480.

**2b** (2″,2″-Dimethyl-3-(3′,5′-difluoromethyl phenyl)-7-acetoxymethyl-2″*H*,3″*H*-4,5-pyrrolo[2,3-*b*]oxazole-8-carboxylic acid methyl ester) is a white solid, with a yield of 40%, melting point ranging from 193.5 to 194.4 °C.· $^1$H NMR (500 MHz, $CDCl_3$) $\delta$ (ppm): $\delta$ 7.94 (s, 1H), 7.76 (s, 2H), 6.60 (s, 1H), 3.97 (s, 3H), 2.73 (s, 2H), 2.33 (s, 3H), 1.40 (s, 6H). $^{13}$C NMR (126 MHz, $CDCl_3$) $\delta$ (ppm): $\delta$ 168.51, 162.91, 158.90, 155.56, 153.56, 151.76, 143.71, 134.32, 130.48, 124.13, 122.68, 121.96, 120.03, 107.79, 107.68, 104.13, 52.89, 37.67, 26.44, 20.85. MS (ESI): *m*/*z*, calculated for $C_{25}H_{18}F_6O_7$ $[M + Na]^+$: 567.0845, found 567.0924.

**2c** (2″,2″-Dimethyl-3-(4′-acetoxyphenyl)-7-acetoxy-2″*H*,3″-4,5-pyranidinocoumarin-8-methylester) is a white solid, with a yield of 41% and melting range of 176.8–178.9 °C. $^1$H NMR (400 MHz, $CDCl_3$) $\delta$ (ppm): $\delta$ 7.32 (d, $J$ = 8.3 Hz, 2H), 7.19 (d, $J$ = 6.7 Hz, 2H), 6.56 (s, 1H), 3.96 (s, 3H), 2.78 (s, 2H), 2.34 (s, 3H), 2.32 (s, 3H), 1.37 (s, 6H). $^{13}$C NMR (126 MHz, $CDCl_3$) $\delta$ (ppm): $\delta$ 169.44, 168.68, 163.17, 159.50, 155.41, 152.80, 150.75, 142.21, 131.33, 129.62, 122.06, 121.75, 107.43, 107.27, 104.67, 103.31, 52.85, 37.79, 26.42, 21.23. MS (ESI): *m*/*z* calculated for $C_{25}H_{22}O_9Na$ $[M + Na]^+$: 489.1143, found 489.4420.

**2.2.3 Preparation of probes 3a, 3b, and 3c.** Under electromagnetic stirring, 100 mL of methanol, compound **2a**, **2b**, **2c**, (3.5 g, 8 mmol) were added successively to a 100 mL round-bottom flask. After heating to complete dissolution, the reaction mixture was cooled to room temperature and transferred to a low-temperature reactor. At 0 °C–5 °C conditions, $NaBH_4$ (1.5 g, 40 mmol) was added in small portions over a period of 1.5 h. The reaction was stirred for an additional 2–4 h, monitored by TLC using petroleum ether and ethyl acetate (3 : 1, v/v) as the eluent until the completion of reaction. Subsequently, 9–10 drops of 5% HCl were added to quench the reaction.After removal of methanol under reduced pressure, then diluted with water and extracted with ethyl acetate (3 × 20 mL). The combined organic layers were successively washed with saturated $NaHCO_3$ solution and saturated brine, dried over

anhydrous sodium sulfate, filtered, and concentrated. The crude product was recrystallized from methanol to obtain compounds **3a**, **3b**, and **3c** with yield was of 65–68%.

**3a** (2′,2′-Dimethyl-3-(4′-chlorophenyl)-7-hydroxy-2″*H*,3″*H*-4,5-pyrrolo[4,5-*b*]chromen-8-carboxylic acid methyl ester) is a white single crystal, with a yield of 68% and melting range of 216.3–217.6 °C. $^1$H NMR (400 MHz, $CDCl_3$) $\delta$ (ppm): $\delta$ 12.25 (s, 1H), 7.45 (d, $J$ = 8.4 Hz, 2H), 7.26 (d, $J$ = 8.4 Hz, 2H), 6.38 (s, 1H), 4.06 (s, 3H), 2.73 (s, 2H), 1.37 (s, 6H). $^{13}$C NMR (126 MHz, $CDCl_3$) $\delta$ 170.43, 167.25, 159.96, 158.16, 154.47, 143.29, 134.44, 131.61, 130.87, 128.80, 118.76, 100.86, 100.16, 95.71, 52.99, 37.89, 26.52. MS (ESI): *m*/*z*, calculated for $C_{21}H_{18}ClO_6$ $[M + H]^+$: 401.0784, found 401.8110.

**3b** (2″,2′-Dimethyl-3-(3′,5′-difluoromethyl phenyl)-7-hydroxy-2″*H*,3″*H*-4,5-pyrrolo[4,5-*b*]chromen-8-carboxylic acid methyl ester): white needle crystals, with a yield of 67% and melting range of 225.1–226.4 °C. $^1$H NMR (500 MHz, $CDCl_3$) $\delta$ (ppm): $\delta$ 12.32 (s, 1H), 7.92 (s, 1H), 7.78 (s, 2H), 6.40 (s, 1H), 4.06 (s, 3H), 2.73 (s, 2H), 1.39 (s, 6H). $^{13}$C NMR (126 MHz, $CDCl_3$) $\delta$ (ppm): $\delta$ 170.27, 167.83, 159.54, 158.25, 154.66, 144.62, 134.66, 130.61, 124.19, 122.36, 122.02, 116.92, 101.21, 99.83, 95.91, 53.03, 37.79, 26.54. MS (ESI): *m*/*z* calculated for $C_{23}H_{17}F_6O_6$ $[M + H]^+$: 503.0923, found 503.3684.

**3c** 2″,2″-Dimethyl-3-(4′-hydroxyphenyl)-7-hydroxy-2″*H*,3″*H*-4,5-pyrrolo[3,4-*b*]carbazole-8-carboxylic acid methyl ester is a white solid with a yield of 65% and a melting point of 162.2–163.6 °C. $^1$H NMR (500 MHz, $CDCl_3$) $\delta$ (ppm): $\delta$ 12.21 (s, 1H), 7.16 (d, $J$ = 7.7 Hz, 2H), 6.89 (d, $J$ = 8.0 Hz, 2H), 6.37 (s, 1H), 5.21 (s, 1H), 4.05 (s, 3H, –$OCH_3$), 2.74 (s, 2H), 1.35 (s, 6H, 2× $CH_3$). $^{13}$C NMR (126 MHz, DMSO-$d_6$) $\delta$ (ppm): $\delta$ 165.86, 160.83, 160.32 157.62, 155.63, 151.88, 142.96, 132.04, 123.43, 119.20, 115.33, 101.56, 99.59, 77.76, 52.86, 37.53, 26.41. MS (ESI): *m*/*z* calculated for $C_{21}H_{19}O_7$ $[M + H]^+$: 383.1125, found 383.3680.

**2.2.4 Crystal data and structure determination of the probe compound.** To further confirm the structure of the target compound, a saturated solution of **3a** in anhydrous ethanol was prepared and allowed to slowly evaporate at room temperature, yielding transparent crystals. A single crystal with dimensions 0.14 × 0.13 × 0.12 mm$^3$ was selected for X-ray diffraction analysis on a Bruker SMART 1000 CCD diffractometer equipped with a graphite-monochromated MoK$\alpha$ radiation source ($\lambda$ = 0.71073 Å). Data were collected at 100.00(10) K using $\omega/2\theta$ scans over a range of 4.806° ≤ 2$\theta$ ≤ 49.986°, yielding 11 039 reflections (3150 unique, $R_{int}$ = 0.0310, $R_{sigma}$ = 0.0328). The data were corrected for Lorentz-polarization (LP) and empirical absorption effects. The crystal structure of **3a** ($C_{21}H_{17}ClO_6$, $M_r$ = 400.80) crystallizes in the monoclinic *C*2/*c* space group, with unit cell parameters $a$ = 23.9515(14) Å, $b$ = 9.1618(4) Å, $c$ = 17.4802(9) Å, $V$ = 3574.2(3) Å$^3$, $D_c$ = 1.490 g cm$^{-3}$, $Z$ = 8, and $F$(000) = 1664.0. The linear absorption coefficient ($\mu$) was 0.252 mm$^{-1}$. The structure was refined by full-matrix least-squares methods using SHELXL-97, yielding final residuals of $R_1$ = 0.0356 and $R_2$ = 0.0987 [for $I > 2\sigma(I)$], with a goodness-of-fit ($S$) of 1.003. The final difference Fourier map showed maximum/minimum residual electron densities of 0.63 e·Å$^{-3}$ and −0.27 e·Å$^{-3}$, respectively.

### 2.3 Preparation and test conditions of experimental materials

**2.3.1 Studies on UV-vis and fluorescence spectroscopy.** Accurately weighed quantities of compounds **2b** and **3c** were dissolved in an acetonitrile-RNA electrophoresis buffer mixture (v/v = 8 : 2) with 5 min of sonication to ensure complete dissolution. The resulting solutions were transferred to 10 mL volumetric flasks and brought to volume, yielding stock solutions with concentrations of 0.002 mM and 0.01 mM, respectively. For analysis, aliquots of each compound solution were pipetted into cuvettes, followed by the addition of 10 μL hydrazinium ion solution. After allowing the reaction to proceed at room temperature for a specified duration, the samples were subjected to UV-Vis spectrophotometry and fluorescence spectroscopy for characterization.

**2.3.2 Anti-interference detection.** Fluorescence intensity responses of probes **2b** and **3c** toward typical cations ($Mg^{2+}$, $Ca^{2+}$, $Zn^{2+}$, $Cu^{2+}$, $Fe^{3+}$, $Na^+$), anions ($Br^-$, $Cl^-$, $ClO_4^-$, $Ac^-$, $HSO_4^-$), and biologically relevant species (glutathione, triethylamine) were systematically investigated.

**2.3.3 Practical application**

*2.3.3.1 Detection of hydrazine vapor.* Accurately weighed quantities of compounds **2b** and **3c** were dissolved in an acetonitrile-RNA electrophoresis buffer mixture (v/v = 8 : 2) to prepare a 10 mM stock solution, and a series of hydrazine hydrate solutions (0, 10, 20, 40, 60, 100, 300, 500 mM, and 1 M) were prepared. Filter paper strips were immersed in **2b**/**3c** test solution for 10 min, air-dried, then spotted with the hydrazine concentration series. After 20–30 min reaction at ambient conditions, the test strips were photo-documented under UV excitation ($\lambda$ = 365 nm).

*2.3.3.2 Detection of hydrazine in food samples (lettuce and rice).* Food samples (rice and lettuce) obtained from local supermarkets were treated by spraying with aqueous $N_2H_4$ solutions (80 mM and 300 mM), followed by surface application of probe solutions **2b** and **3c** (10 mM). The samples were then photo-documented under controlled lighting conditions to record the detection response.

### 2.4 DFT calculations

Density functional theory (DFT) was used to optimize the ground state geometry of the probe **2b** and **3c** using cam-b3lyp/6-311+g(d,p), m06-2x/def2svp, and pbe0/6311+g(d,p), respectively. The optimal functional and basis set were selected. Based on the optimized ground state geometric structure, excited state correlation calculations were performed using TD-DFT. All these calculations were performed using Gaussian 16.

## 3 Results and discussion

### 3.1 Design and synthesis of probe 2(a–c) and 3(a–c)

The synthetic route of this study is illustrated in Scheme 1. Using 2,4,6-trihydroxybenzoic acid methyl ester and 3,3-dimethylacrylic acid starting materials, a novel class of angular pyranocoumarin scaffold was synthesized through PPA-mediated cyclization, Perkin condensation, and reduction, affording

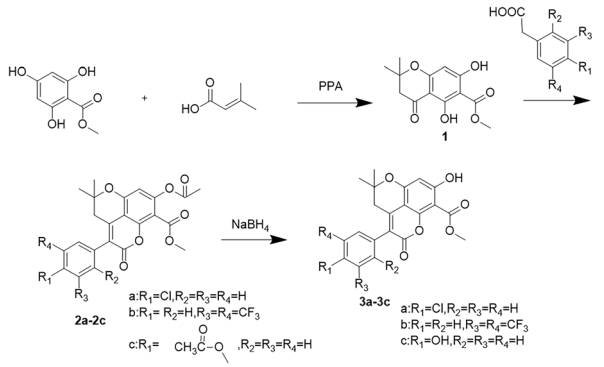


Scheme 1 Synthesis of the probes (**2a–2c**) and (**3a–3c**).

a series of of 3-aryl-4,5-pyranocoumarin derivatives with monoester or diester functional groups (**2a–2c** and **3a–3c**). To date, no literature has reported on the 4,5-pyranocoumarin scaffold or its synthesis methods, representing the first discovery of this study. Additionally, the single crystal of compound **3a** was successfully prepared using anhydrous ethanol as the solvent, and its structure was characterized by X-ray single crystal diffraction technology.

The molecular structure of **3a** is shown in Fig. 3(A), and the packing diagram of **3a** is depicted in Fig. 3(B). Most bond lengths in the system fall in the range of single and double bonds and the C–C bond distances in all rings range between 1.358 (2) and 1.522 (2) Å, almost equal to the values of typical bonds of aromatic structure. 3-Aroyl is almost coplanar with the torsion angles of C13–C12–C3–C2 to be −119.45(17) °. During the structural analysis, it was found that an intramolecular hydrogen bond was formed between O5–H and O6, with a bond length of 2.551 Å. In the crystal packing diagram, the centroid-to-centroid distance of the C5–C10–C9–C8–C7–C6 aromatic plane is 3.632 Å, with a lateral displacement of 1.527 Å. These values suggest a slipped π–π stacking interaction between molecules. The centroid-to-centroid distance falls within the typical range for π–π interactions in aromatic systems (3.3–3.8 Å), while the significant lateral displacement (approximately 42% of the centroid-to-centroid distance) indicates that the molecular planes are not fully overlapped but rather exhibit a partially offset arrangement. This configuration optimizes van der Waals interactions between molecules. Such a packing mode effectively balances π–π attraction and steric repulsion, thereby enhancing the overall stability of the crystal structure.

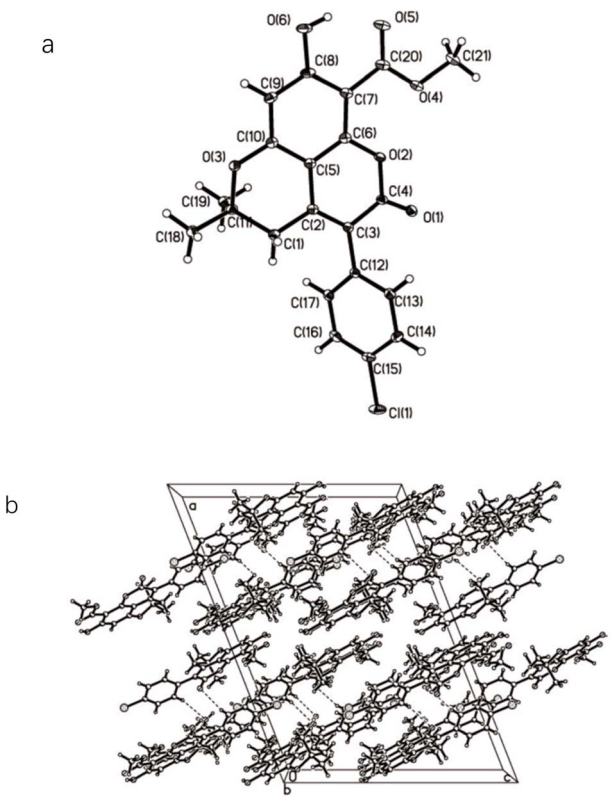


Fig. 3 (a) X-ray single crystal diffraction diagram of compound **3a**; (b) the packing of **3a**, viewed down the *b* direction (CCDC 2449340).

### 3.2 Optical responses of compounds 2(a–c) and 3(a–c) to $N_2H_4$

Selectivity is a critical parameter for assessing probe performance, as only probes with high selectivity possess practical application value. In this study, we evaluated the potential interference from several common cations ($Mg^{2+}$, $Ca^{2+}$, $Zn^{2+}$, $Cu^{2+}$, $Fe^{3+}$, $Na^{+}$), anions ($Br^{-}$, $Cl^{-}$, $ClO_4^{-}$, $Ac^{-}$, $HSO_4^{-}$), and small molecules (glutathione (GSH), triethylamine (TEA)) using fluorescence spectroscopy. As shown in Fig. 4, the fluorescence intensity of probe **2b** at 424 nm (∼8000 a.u.) was dramatically enhanced to 23 616 a.u. upon treatment with $N_2H_4$, representing a 195% increase. Probe **3c** exhibited more superior response characteristics, with its fluorescence intensity at 460 nm surging from 4423 a.u. to 26 275 a.u. (a 494% increase) in the presence of $N_2H_4$, and a new fluorescence emission peak emerged at 462 nm. No significant responses were observed with other ions or small molecular reagents, and both probes demonstrated excellent selectivity to $N_2H_4$. Conversely, compounds **2a** and **3a** did not show significant changes in fluorescence intensity after the addition of hydrazine, but it exhibited obvious quenching effects in the presence of $Cl^{-}$, $HSO_4^{-}$, $ClO_4^{-}$, $Ac^{-}$, $Br^{-}$ or $Zn^{2+}$. Compound **2c** not only exhibits quenching effects on $N_2H_4$, but also on triethylamine (TEA), $Zn^{2+}$ and $Cu^{2+}$. Compound **3b** aslo exhibits a significant quenching effect on $N_2H_4$ and TEA. Thus, only **2b** and **3c** demonstrate sufficient selectivity for hydrazine detection and was chosen for further studies.

UV-Vis spectroscopy of representative compound **2b** and **3c** (Fig. 4g and h) also further demonstrated their ability to bind with $N_2H_4$. The results indicate that probe **2b** exhibits characteristic absorption peaks at 255 nm and 310 nm. Upon the addition of $N_2H_4$, the absorption intensity significantly increases, accompanied by a red shift in the maximum absorption wavelength (310 nm → 325 nm), suggesting an interaction between the probe and $N_2H_4$. Additionally, the

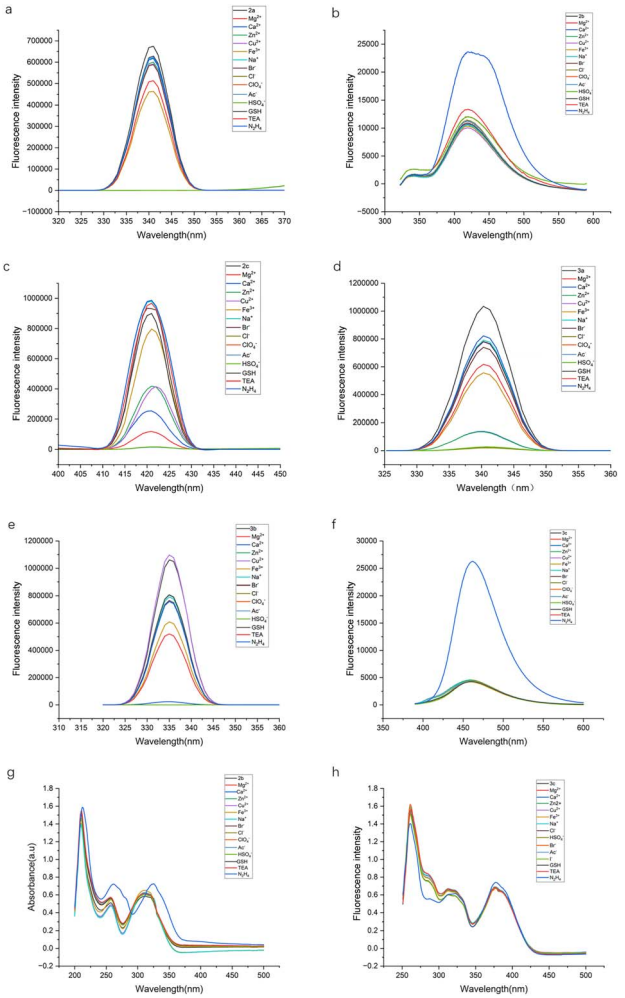

Fig. 4 (a–f) Fluorescence response profiles of compounds **2a–2c** and **3a–3c** in the presence of common cations ($Mg^{2+}$, $Ca^{2+}$, $Zn^{2+}$, $Cu^{2+}$, $Fe^{3+}$, $Na^{+}$), anions ($Br^{-}$, $Cl^{-}$, $ClO_4^{-}$, $Ac^{-}$, $HSO_4^{-}$), and biological reagents (GSH, TEA). (g and h) UV-Vis spectrum of **2b** and **3c** in the presence of common cations ($Mg^{2+}$, $Ca^{2+}$, $Zn^{2+}$, $Cu^{2+}$, $Fe^{3+}$, $Na^{+}$), anions ($Br^{-}$, $Cl^{-}$, $ClO_4^{-}$, $Ac^{-}$, $HSO_4^{-}$), and biological reagents (GSH, TEA).

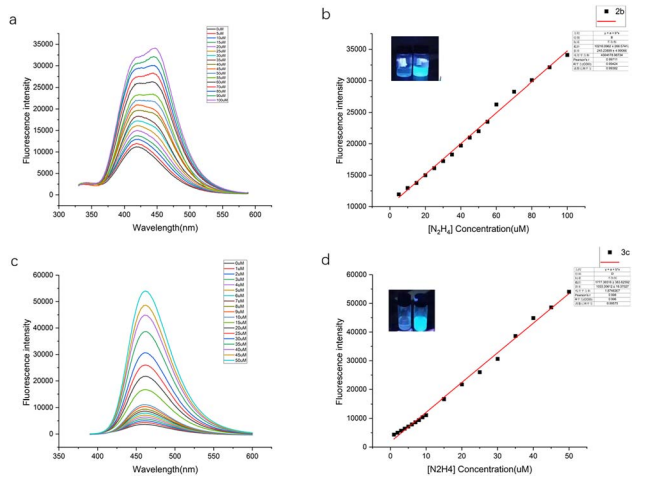

Fig. 5 (a and c) Fluorescence spectra of probe **2b** and **3c** (0.1 mM) in the presence of varying concentrations of $[N_2H_4]$ (0–100 μM/0–50 μM). (b and d) Fluorescence intensity graph of probe **2b/3c** with hydrazine (0–100 μM/0–50 μM).

characteristic absorption peak of probe **3c** at 325 nm also demonstrates a pronounced hyperchromic effect. It is noteworthy that the influence of common cations ($Mg^{2+}$, $Ca^{2+}$, $Zn^{2+}$, $Cu^{2+}$, $Fe^{3+}$, $Na^{+}$), anions ($Br^{-}$, $Cl^{-}$, $ClO_4^{-}$, $Ac^{-}$, $HSO_4^{-}$), and biological reagents (GSH, TEA) on the absorbance of the two probes is significantly lower than that of $N_2H_4$, confirming the probes' high binding selectivity for $N_2H_4$.

The relationship between hydrazine and fluorescence intensity was systematically investigates. As shown in Fig. 5, probes **2b** ($R = 0.99398$) and **3c** ($R = 0.99554$) both exhibit a good linear relationship with varying concentrations of hydrazine hydrate (0–50 μM or 0–10 μM). As hydrazine is gradually added, compound **2b** exhibits a concentration-dependent fluorescence enhancement at 424 nm, accompanied by a significant red shift phenomenon ($\Delta\lambda = 18$ nm), with the emission peak shifting to 442 nm. Compound **3c** shows a gradual increase in fluorescence intensity at 457 nm, without any observed change in wavelength. Based on the detection limit calculation formula $\mathrm{LOD} = 3\sigma/K$ (where $\sigma$ represents the standard deviation and $K$ represents the slope of the calibration curve), it was determined that $\sigma = 7.49$. The detection limits for probe **2b** and probe **3c** were calculated to be 0.12 μmol $L^{-1}$ and 0.03 μmol $L^{-1}$, respectively. According to the literature,[24–27] the detection limit of probe **3c** is lower than most reported coumarin-based fluorescent probe for hydrazine detection and is significantly below the standard upper limit (0.03 μM) established by the United States Environmental Protection Agency (EPA). These results indicate that probes **2b** and **3c** possess high sensitivity and low detection limits for the recognition of hydrazine ions, making them suitable for detecting trace hydrazine concentrations in actual samples.

To evaluate the selectivity of probes **2b** and **3c** for hydrazine against potential interferents, we systematically examined their changes in fluorescence intensity in the existence of the common cations ($Na^{+}$, $Mg^{2+}$, $Ca^{2+}$, $Zn^{2+}$, $Cu^{2+}$, $Fe^{3+}$), anions ($Cl^{-}$, $Br^{-}$, $ClO_4^{-}$, $HSO_4^{-}$, $Ac^{-}$), and biologically relevant species (glutathione, triethylamine). As shown in Fig. 6(a and b), except for triethylamine (a slight fluorescence enhancement), the other analytes had no significant impact on the fluorescence intensity of probe **2b** after addition of hydrazine. Probe **3c** did not exhibit any significant changes in fluorescence response in the presence of all tested interferents, fully confirming its highly specific recognition capability for hydrazine.

This study also systematically examined the stability of probes **2b** and **3c** under different pH conditions (Fig. 6e and f). The results demonstrated that compound **2b** exhibited stable fluorescence intensity over a pH range of 1 to 12. However, under conditions of pH > 8, its fluorescence intensity gradually increased with increasing pH. This might be attributed to the gradual hydrolysis of the ester group of compound **2b** in

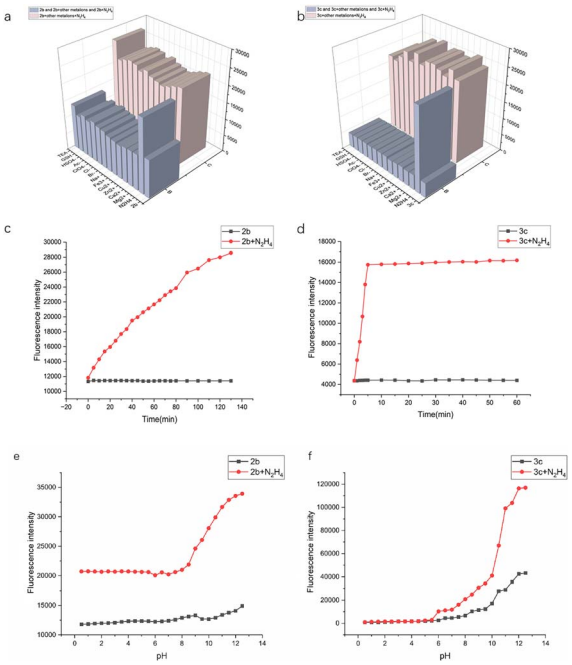


Fig. 6 (a) Fluorescence intensity profile of probe **2b** toward hydrazine ($[N_2H_4]$) in the presence of various competing ions (*e.g.*, $Mg^{2+}$, $Ca^{2+}$, $Cl^-$, GSH). (b) Time-dependent fluorescence intensity changes of **2b** (control) and **2b** + $[N_2H_4]$ over 0–140 min. (c) Corresponding fluorescence response of probe **3c** for hydrazine detection under identical interference conditions. (d) Comparative fluorescence intensity profiles of **3c** and **3c** + $[N_2H_4]$ within 0–60 min. (e) pH-dependent fluorescence intensity variations of **2b** and **2b** + $[N_2H_4]^+$ across the pH range 0–13 (f) pH-dependent fluorescence intensity changes of **3c** and **3c** + $[N_2H_4]$ under the same pH 0–13 conditions.

a strongly alkaline environment. After adding hydrazine, the fluorescence intensity of compound **2b** significantly increased and remained stable within the pH range of 1–8. But in alkaline condition (pH > 8), its fluorescence intensity increased with the rise of pH and reached a constant value at pH = 12. This phenomenon may be related to the fact that coumarins (especially their two ester groups) undergo a chemical reaction with hydrazine under alkaline conditions and generate new substances. Compound **3c** exhibited stable fluorescence performance over a pH range of 1 to 6. However, under pH value of over 6, its fluorescence intensity gradually increased until pH 12. The ester group of probe **3c** remains stable under acidic conditions and shows low reactivity. Following the addition of hydrazine hydrate, only a minor change in fluorescence intensity was observed, suggesting that acid addition can suppress the hydrazine hydrate-induced fluorescence enhancement.

Fluorescence stability tests for probes **2b** and **3c** ($2 \times 10^{-6}$ mol $L^{-1}$) were performed every 10 minutes in acetonitrile-RNA electrophoresis buffer (8 : 2, v/v). The fluorescence intensities at their respective maximum emission peaks (424 nm for **2b**, 462 nm for **3c**) showed no significant changes within 1 hour. This confirms the probes' stability under the experimental conditions, validating the reliability of the results and minimizing potential errors from probe instability. Upon addition of

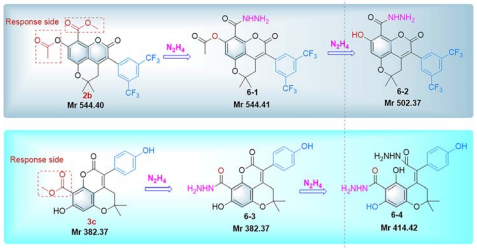


Scheme 2 The response mechanism of probe **2b** and **3c** to hydrazine hydrate.

$N_2H_4$, the fluorescence intensity of probe **2b** increased continuously but did not stabilize within 140 minutes. In contrast, probe **3c** reached its maximum intensity within 5 minutes and remained stable thereafter.

### 3.3 The recognition mechanism of $N_2H_4$ by probe 2b and 3c

The reaction mechanism of ester-based fluorescent probes in the detection of hydrazine usually involves the specific reaction between the ester bond in their molecular structure and hydrazine (Scheme 2). This reaction cleaves one ester bond to form hydrazide derivative 6–1 while hydrolyzing the other ester group to yield hydroxyl-containing product 6–2. The subsequent release of the fluorophore/chromophore moiety generates significant fluorescence enhancement. HRMS analysis (Fig. 7a and b) confirms this mechanism: probe **2b** displays a $[M + Na]^+$ peak at *m/z* 567.0851 ($ESI^+$), whereas after reaction with $N_2H_4$, a $[M + H]^+$ peak at *m/z* 503.1966 corresponding to product 6–2 is observed.

At the same time, probe **3c** exhibits a similar reaction mechanism. However, due to the presence of only one ester group, the amino group of $N_2H_4$ not only attacks the carbonyl carbon atoms of the ester moiety in probe **3c**, leading to the formation of the coumarin amide hydrazide, but also further

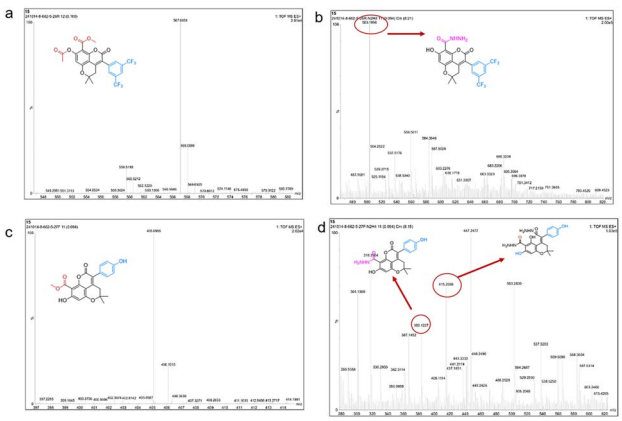


Fig. 7 HRMS of **2b** (a) in the absence and (b) in the presence of hydrazine hydrate; HRMS of **3c** (c) in the absence and (d) in the presence of hydrazine hydrate.

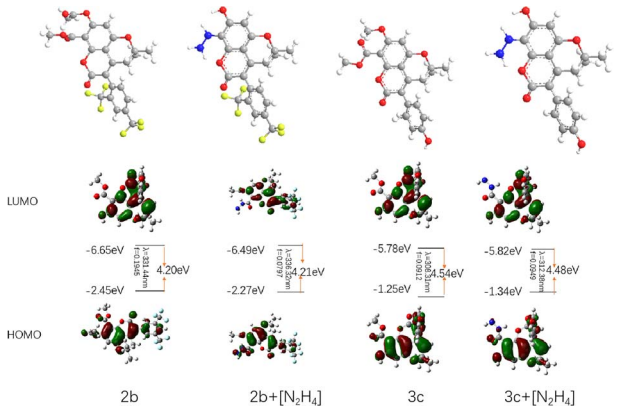


Fig. 8 Computational analysis of probes **2b**/**3c** by density functional theory (DFT).

interacts with the coumarin lactone ring, resulting in ring rupture. According to the HRMS analysis results (Fig. 7c and d), probe **3c** displays a $[M + Na]^+$ peak (*m*/*z* 405.0955) in positive ion mode ($ESI^+$). Upon the addition of hydrazine, the $[M + H]^+$ peak (*m*/*z* 383.1227) corresponding to the coumarin hydrazide product **6-3** and the $[M + H]^+$ peak (*m*/*z* 415.2096) associated with the product **6-4** after ring rupture are generated.

To deeply explore the mechanism of fluorescence enhancement, the interaction between probes and $N_2H_4$ was systematically analyzed through density functional theory (DFT) calculations (Fig. 8).

After binding with $N_2H_4$, both the HOMO and LUMO energy levels of probe **2b** shifted towards higher energies (HOMO: −2.45 → −2.27 eV; LUMO: −6.65 → −6.49 eV), indicating that the introduction of $N_2H_4$ reconstructed the electronic structure of the probe through electron donor effects. Although the HOMO–LUMO energy gap only slightly increased from 4.20 eV to 4.21 eV (a change of 0.01 eV), the oscillator strength (*f*-value) drastically decreased from 0.194 to 0.0797 (a reduction of 59%), a phenomenon that significantly impacts fluorescence properties. Experimental datas reveal that probe **2b** exhibits a red shift in fluorescence emission from 424 nm to 442 nm. Despite minimal energy gap variation, this shift may be attributed to elevated HOMO/LUMO energy levels altering intramolecular charge transfer (ICT) characteristics.

After combination of probe **3c** with $N_2H_4$, its HOMO level decreased from −1.25 eV to −1.34 eV, and the LUMO level decreased from −5.78 eV to −5.82 eV. The HOMO–LUMO gap narrowed by 0.06 eV (from 4.54 eV to 4.48 eV), while the oscillator strength (*f*-value) increased from 0.0912 to 0.0949. This phenomenon contrasts sharply with the significant decrease in the *f*-value observed in probe **2b**, highlighting the differences in the action mechanisms of various probes. The contraction of the energy gap reduces the energy difference between the ground state and the excited state, leading to an increased Stokes shift and a red shift in fluorescence emission. However, neither UV nor fluorescence spectra exhibited a significant red shift. This absence may stem from solvent effects or compensation by other factors. Meanwhile, the increase in the *f*-value (by 4.1%) enhances the probability of radiative transition,

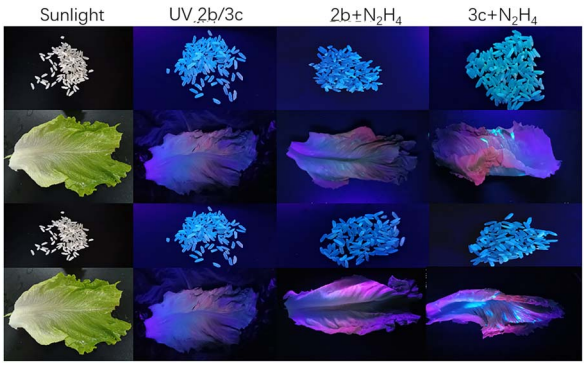


Fig. 9 UV-Vis and sunlight response of probes **2b**/**3c** toward hydrazine in food matrices paper.

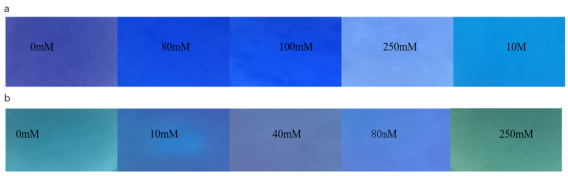


Fig. 10 (a) Filter paper assay of probe **2b** at graded concentrations. (b) Filter assay of probe **3c** at graded concentrations.

thereby increasing fluorescence intensity, consistent with the experimental results.

This study further demonstrated the practical detection capabilities of probes **2b** and **3c** in simulated food samples. A 10.0 mM probe solution was uniformly sprayed on pretreated rice and lettuce surfaces, followed by localized application of 80 mM hydrazine hydrate to simulate contamination. Under UV light (365 nm) imaging, hydrazine-exposed areas exhibited a distinct blue or cyan fluorescence transition with both probes, generating high-contrast spatially resolved signals. Notably, probe **3c** demonstrated significantly higher fluorescence enhancement intensity than **2b**, indicating superior detection sensitivity (Fig. 9). These experiments confirmed that both probes enable visual monitoring of hydrazine contamination on food surfaces without complex sample pretreatment. In particular, **3c** was exhibited significant fluorescence emission changes and rapid response performance.

Based on the aforementioned spectral performance advantages, this study further validated the practical application potential of probes **2b** and **3c** through a visual test strip experiment. As shown in Fig. 10, the experiment utilized the impregnation method to prepare probe-loaded test strips, which were then exposed to hydrazine vapor at varying concentrations. The results demonstrated that under 365 nm UV light excitation, the test strip loaded with probe **2b** exhibited purple fluorescence, while the strip loaded with probe **3c** displayed blue-green fluorescence. As the hydrazine concentration increased, the fluorescence intensity of the test strip loaded with probe **2b** gradually intensified, showing a distinct blue fluorescence at a concentration of 10 M. Conversely, the test strip loaded with probe **3c**

exhibited a color transition from blue-green to blue and then to green. Notably, the test strip loaded with probe **3c** displayed a more significant response in terms of fluorescence enhancement, requiring only 250 mM of hydrazine hydrate to induce a noticeable change in the filter paper.

## 4 Conclusions

In summary, this study successfully designed and synthesized two novel 3-aryl-4,5-pyranocoumarin-based fluorescent probes (**3c** and **2b**) with fully characterized structures by $^{1}H/^{13}C$ NMR and HRMS. The structural uniqueness of the 4,5-pyranocoumarin skeleton was confirmed through X-ray crystallography, which revealed intramolecular hydrogen bonding and slipped π–π stacking interactions, both of which stabilize the crystal lattice. Both probes exhibited exceptional selectivity and sensitivity towards hydrazine ($N_2H_4$), with **3c** achieving an ultralow detection limit of 0.03 μM, surpassing most reported probes and meeting the stringent EPA standard of 10 ppb. Mechanistic studies demonstrated that $N_2H_4$ induces ester bond cleavage and structural rearrangement, resulting in fluorescence activation and intramolecular charge transfer (ICT) modulation, as corroborated by HRMS analysis and DFT calculations. While **2b** displayed broader pH adaptability (pH 1–12) and a red-shifted emission ($\Delta\lambda = 18$ nm), **3c** demonstrated superior performance in terms of specificity, rapid response time, and resistance to some interferents. Practical validation in food matrices and test strips underscored their potential for on-site hydrazine detection, with **3c** demonstrating superior sensitivity and visual signal contrast. This work not only propels the advancement of pyranocoumarin-based optical sensors, but also establishes a versatile platform for environmental and food safety monitoring field-deployable sensors, for accurate hydrazine quantification across environmental and food safety applications.

## Author contributions

Huafeng Zhou and Jiayong Huang: investigation, experimental operation, software, writing-original draft, formal analysis; Jian Su: investigation, experimental assistance; Xiaowei Su: investigation, data curation, formal analysis; Qiujuan Chen: investigation, data curation, formal analysis; Yuxiao Zheng: experimental assistance, data curation; Rui Chen and Lini Huo: revising the paper and supervising the research. All authors approved the final version of the publication.

## Conflicts of interest

There are no conflicts to declare.

## Data availability

CCDC 2449340 (**3a**) contains the supplementary crystallographic data for this paper.[28]

Data is provided within the manuscript or SI files. Supplementary information: we have presented all our main data in the form of tables and figures. See DOI: https://doi.org/10.1039/d5ra04433b.

## Acknowledgements

This work is funded by Natural Science Foundation of Guangxi Province (2023GXNSFAA026476), the Project Program of Guangxi Key Laboratory of Drug Discovery and Optimization (GKLPMDDO2022B02), Qihuang High-level Talent Team Cultivation Project of Guangxi University of Chinese Medicine (202405), Inheritance and Innovation team of Guangxi Traditional Chinese Medicine (2022B005).

## Notes and references

1 M. I. Tenevich, A. P. Shevchik and V. I. Popkov, *J. Sol-Gel Sci. Technol.*, 2022, **101**(2), 380–389.
2 S. A. A. M. Sarhan, M. Haukka, A. Barakat, *et al.*, *Crystals*, 2023, **13**(11), 1537.
3 R. Saida, T. Shimizu, T. Ito, *et al.*, *J. Electron. Mater.*, 2023, DOI: 10.1007/s11664-023-10605-5.
4 W. Jia, X. Wang, Z. Lu, *et al.*, *J. Alloys Compd.*, 2021, DOI: 10.1016/j.jallcom.2021.160990.
5 Q. Lai, S. Si, T. Qin, *et al.*, *Sens. Actuators, B*, 2020, **307**, 127640.
6 S. Mu, H. Gao, C. Li, *et al.*, *Talanta*, 2021, **221**, 121606.
7 A. Mohammad, M. E. Khan, I. M. Alarifi, *et al.*, *Microchem. J.*, 2021, **171**, 106784.
8 K. Ke, D. Wei, Z. Lu, *et al.*, *Sens. Actuators, B*, 2023, **395**, 134456.
9 X. Qin, M. Lin, Z. Lai, *et al.*, *Dyes Pigm.*, 2024, **231**, 112378.
10 T. T. Zhang, Construction and application of a new hydrazine hydrate fluorescent probe, Master's thesis, Guangxi University, 2023.
11 K. Pršir, E. Horak, M. Kralj, *et al.*, *Molecules*, 2022, **27**(3), 637–652.
12 X. Y. Sun, T. Liu, J. Sun, *et al.*, *RSC Adv.*, 2020, **10**(18), 10826–10847.
13 X.-L. Hu, H.-Q. Gan, F.-D. Meng, *et al.*, *Front. Chem. Sci. Eng.*, 2022, DOI: 10.1007/s11705-022-2163-1.
14 T. T. Hao, Construction and Application of a Coumarin-Based Hydrogen Sulfide Fluorescent Probe, Master's thesis, Hebei University, 2024.
15 F. Yang, L. Yang, L. Xu, *et al.*, *Microchim. Acta*, 2021, **188**(9), 04965.
16 X. Wang, J. Zhang, J. Zhu, *et al.*, *Anal. Methods*, 2022, **14**(23), 2284–2292.
17 W. Xu, X. Li, J. Yin, *et al.*, *Anal. Sci.*, 2019, **35**(12), 1341–1345.
18 X. Xia, F. Zeng, P. Zhang, *et al.*, *Sens. Actuators, B*, 2016, **227**, 411–418.
19 G. Tlan, Z. X. Zhang, H. D. Li, *et al.*, *Crit. Rev. Anal. Chem.*, 2021, **51**(6), 565–581.
20 G. Liang-Liang, P. Shulin, G. Ying, *et al.*, *Adv. Agrochem*, 2022, **1**(1), 22–38.
21 K. Zuo, Construction and Detection Performance of Hydrazine Hydrate Fluorescence Test Paper, Master's thesis, Guangxi University, 2023.

22 Y. H. Dai, Y. M. Zhao, M. Y. Zhang, *et al.*, *Shandong Chem. Ind.*, 2021, **50**(4), 30–31.
23 S. Niyazi, B. Pouramiri and K. Rabiei, *J. Mol. Struct.*, 2022, **1250**, 131908.
24 J. H. Xie, L. Wang, X. Q. Su, *et al.*, *Curr. Org. Chem.*, 2021, **25**(18), 2142–2154.
25 P. Qu, X. Ma, W. Chen, *et al.*, *Spectrochim. Acta, Part A*, 2019, **210**, 381–386.
26 T. Li, J. Liu, L. Song, *et al.*, *J. Mater. Chem. B*, 2019, **7**(20), 3197–3320.
27 J. H. Xie, L. Wang, X. Q. Su, *et al.*, *Curr. Org. Chem.*, 2021, **25**(18), 2142–2154.
28 H. Zhou, J. Huang, J. Su, X. Su, Q. Chen, R. Li, Y. Zheng, R. Chen and L. Huo, CCDC 2449340: Experimental Crystal Structure Determination, 2025, DOI: **10.5517/ccdc.csd.cc2n6qzl**.